In-Plane Forces Prediction and Analysis in High-Speed Conditions on a Contra-Rotating Open Rotor

Benjamin François
Aerodynamic Department,
Airbus Operations S.A.S.,
306 Route de Bayonne,
Toulouse Cedex 9 31000, France
e-mail: benjamin.francois@cerfacs.fr

Martin Laban
Flight Physics and Loads Department,
National Aerospace Laboratory, NLR,
Anthony Fokkerweg 2,
Amsterdam 1059CM, Netherlands
e-mail: martin.laban@nlr.nl

Michel Costes
Onera, The French Aerospace Lab,
8 Rue des Vertugadins,
Meudon F-92190, France
e-mail: michel.costes@onera.fr

Guillaume Dufour
Institut Supérieur de l'Aéronautique
et de l'Espace (ISAE),
Université de Toulouse, 10 avenue Edouard
Belin, 31400 Toulouse, France
e-mail: guillaume.dufour@isae.fr

Jean-François Boussuge
CFD Department, CERFACS,
42 avenue Gaspard Coriolis,
31000 Toulouse, France
e-mail: boussuge@cerfacs.fr

Due to the growing interest from engine and aircraft manufacturers for contra-rotating open rotors (CROR), much effort is presently devoted to the development of reliable computational fluid dynamics (CFD) methodologies for the prediction of performance, aerodynamic loads, and acoustics. Forces transverse to the rotation axis of the propellers, commonly called in-plane forces (or sometimes 1P forces), are a major concern for the structural sizing of the aircraft and for vibrations. In-plane forces impact strongly the stability and the balancing of the aircraft and, consequently, the horizontal tail plane (HTP) and the vertical tail plane (VTP) sizing. Also, in-plane forces can initiate a flutter phenomenon on the blades or on the whole engine system. Finally, these forces are unsteady and may lead to vibrations on the whole aircraft, which may degrade the comfort of the passengers and lead to structural fatigue. These forces can be predicted by numerical methods and wind tunnel measurements. However, a reliable estimation of in-plane forces requires validated prediction approaches. To reach this objective, comparisons between several numerical methods and wind tunnel data campaigns are necessary. The primary objective of the paper is to provide a physical analysis of the aerodynamics of in-plane forces for a CROR in high speed at nonzero angle of attack using unsteady simulations. Confidence in the numerical results is built through a code-to-code comparison, which is a first step in the verification process of in-plane forces prediction. Thus, two computational processes for unsteady Reynolds-averaged Navier–Stokes (URANS) simulations of an isolated open rotor at nonzero angle of attack are compared: computational strategy, open rotor meshing, aerodynamic results (rotor forces, blades thrust, and pressure distributions). In a second step, the paper focuses on the understanding of the key aerodynamic mechanisms behind the physics of in-plane forces. For the front rotor, two effects are predominant: the first is due to the orientation of the freestream velocity, and the second is due to the distribution of the induced velocity. For the rear rotor, the freestream velocity effect is reduced but is still dominant. The swirl generated by the front rotor also plays a major role in the modulus and the direction of the in-plane force. Finally, aerodynamic interactions are found to have a minor effect

1 Introduction

In the context of increasing costs for fuel, the development of new aircraft designs is mainly driven by the need to reduce fuel burn. To reach this end, new engine concepts such as contra-rotating open rotors appear to be one suitable option for the single aisle segment, currently dominated by the Airbus A320 and Boeing 737. This concept was the focus of a large research effort led by NASA and US industry in the late 1970s and 1980s, motivated by the high fuel costs arising from the 1973 oil crisis [1]. Significant advances were achieved, but due to the decrease in oil prices, the interest in bringing those engines to market waned. Presently, the CROR concept appears again to be one promising option for powering the new generation of short-range aircraft.

This new concept raises major challenges for aircraft manufacturers. One of them is the impact of forces transverse to the rotation axis of the propellers, commonly named in-plane forces[1], which are caused by a nonhomogeneous inflow velocity flow field in the propeller plane. Such conditions are encountered when the far-field inflow has an angle of attack with respect to the rotation axis (incidence, sideslip) or for an installed propeller configuration. Therefore, it is essential to predict these forces for the structural design of the installed engine system. In-plane forces contribute also to the sizing of HTP and VTP because these forces need to be counterbalanced to meet handling quality requirements. Then, in-plane forces can initiate a flutter phenomenon on the blades or on the whole engine system. Finally, these forces are unsteady and may lead to vibrations on the whole aircraft that may degrade the comfort of the passengers and lead to structural fatigue.

In order to predict accurately the in-plane forces on open rotors, a lot of effort is devoted to the development and the validation of methods and tools for high-fidelity aerodynamic simulations and to wind tunnel test campaigns on open rotor configurations. The work presented in this paper focuses on the assessment and the understanding of in-plane forces on an isolated open rotor configuration at high-speed (conditions in which in-plane force magnitude can reach the same order of the thrust level) at nonzero angle of attack.

Numerous works have been done in the past to predict and understand the origin of the in-plane forces around propellers. The in-plane forces on propellers at nonzero angle of attack were pointed out for the first time in 1909 by Lanchester [2]. A few years later, the first basic theories emerged with Harris [3] and Glauert [4] who proposed an analogy with a fin: A propeller at

Contributed by the International Gas Turbine Institute (IGTI) of ASME for publication in the JOURNAL OF TURBOMACHINERY. Manuscript received January 17, 2013; final manuscript received December 11, 2013; published online January 31, 2014. Assoc. Editor: Alok Sinha.

[1]The expression *1P-forces* (1P stands for once-per-revolution) can also be found in literature to define the in-plane forces on a propeller. However, the 1P-forces expression will not be used in this work.

nonzero angle of attack develops a normal force in the orthogonal direction of the incoming velocity vector as a fin. Forces and moments arising were expressed with an analytical expression using the thrust and torque of an uninclined propeller. Forces applied on propellers were split into the forces along the rotation axis, commonly called thrust, and the force normal to the rotation axis. In 1935, Glauert [5] proposed a widely used analytical expression of the normal force. For an inclined propeller, this force is a function of the angle of inclination, the advance ratio J, the power coefficient C_p, and the thrust distribution along the blade. Glauert's definition considered only the component contained in the vertical plane for an inclined propeller. Lateral force was not taken into account. Comparison of Glauert's theory to experimental results [6] showed little discrepancies, but this validation was limited up to blade settings angles of 45 deg and advance ratio value of 2.0. Later, this theory was exploited by Ribner [7] who extended it to contra-rotating propellers. From the 1950s to the 1980s, fewer articles about propellers were published, probably due to a decreasing interest in propellers and the emergence of the turbofan technology. These analytical models were rapid methods for the improvement of propellers aerodynamics but were not valid for compressible flows.

After the oil crisis, many studies on propellers reemerged in the 1980s with the first three-dimensional steady Euler computations at high speed with the work of Bober et al. [8]. The move to computational procedures for solving the fluid dynamic equations was motivated by two main reasons. First, analytical models were only valid at low-speed and, thus, unfit for transonic flows. Second, Euler computations were accurate means of determining the aerodynamic characteristics of a complex blade for which the three-dimensional geometry cannot be handled by existing analytical models. The computations of Bober et al. were performed on isolated propellers at zero angle of attack. The computational domain was reduced to a single blade passage with periodicity boundary conditions. The flow was solved with a steady approach in the rotating frame. Comparison with experiments showed that the power coefficient is overpredicted, but the variation regarding its blade angle was well captured. According to Bober et al., these discrepancies could be attributed to the viscous effects. These methods were extended to contra-rotating propellers by Wong et al. [9] and Nicoud et al. [10]. The rotor-rotor interface was modeled with a mixing-plane condition [11]. First aerodynamic simulations of propellers at nonzero angle of attack at high-speed (Mach number from 0.6 to 0.8) were achieved by Nallasamy [12] in 1994. All the blades have to be accounted for in the computation because there are no flow periodicity relations. The flow was solved with an unsteady approach because the inflow seen by the blade varies depending on its azimuthal position. Pressure transducers measurements over a rotation for different radii were compared to the numerical simulation results and showed acceptable discrepancies. Nonetheless, nonlinear variations of the measured pressure were not reproduced by the numerical procedure. Then, unsteady Euler computations of high-speed propellers with aircraft were simulated by Bousquet and Gardarein [13] and were compared to wind tunnel in-plane forces measurements at Mach number 0.7. The comparison showed that normal and lateral forces were underpredicted by 15–20%.

Improvements in numerical simulations made it possible to account for the viscous effects using a Navier–Stokes solver to study the propellers' aerodynamics. First, Stuermer [14] achieved advanced three-dimensional Navier–Stokes simulations on isolated open rotors focusing on the aerodynamic performance and in-plane forces at low-speed and high-speed. Zachariadis and Hall [15] focused on the prediction of the rotor performance by investigating the best numerical settings (mesh strategy, boundary conditions) and by comparing them with wind tunnel measurements. These enhancements in the computational approach allowed focus on the acoustic prediction [16,17] and on the prediction of performance and in-plane forces on installed open rotor configurations [18,19]. An important contribution for the simulation of open-rotors at nonzero angle of attack is the work of Brandvik et al. [20]. It focuses on the interaction of the front rotor wake and tip vortex with the rear rotor for acoustic purposes. However, to the authors' knowledge, no numerical prediction of the in-plane forces on an open rotor was compared to experimental data. Ortun et al. [21] performed such a comparison but only on an isolated single propeller. In-plane forces results matched quite well with experimental measurements at low-speed but presented larger discrepancies at high-speed, which are not fully understood. In the same work, Ortun et al. [21] also presented an analysis of the origin of the normal and lateral component of in-plane forces applied on a single propeller. Such an analysis was never performed before and enables us to understand which aerodynamic phenomena are at stake. The use of the lifting-line technique coupled with an unsteady wake model (gathered in the HOST code [22]) enable us to deepen and separate the different in-plane forces contributions. However, this comparison and this analysis have never been applied to contra-rotating open rotors.

In this context, the primary objective of this contribution is to provide a physical analysis of the aerodynamics of in-plane forces for a CROR in high speed at nonzero angle of attack using unsteady simulations. High-speed conditions are selected, as they are one of the most critical for an aircraft with respect to in-plane forces because their magnitude can reach the same order as the thrust level in these conditions. As no validation data are available, confidence in the numerical results is built through a code-to-code comparison. This is a first step in the verification process of in-plane forces prediction, consolidating the reliability of the CFD results. Thus, two computational processes for URANS simulations of an isolated open rotor at nonzero angle of attack are compared: computational strategy, open rotor meshing, and aerodynamic results. The comparisons focus on rotor forces, blades thrust, and pressure distributions.

In the second part of this work, an in-depth analysis of the mechanisms contributing to the in-plane forces is proposed. The results of the simulations are used to identify and explain the key aerodynamic phenomena leading to in-plane forces for each stage. Their contributions to the different components (modulus, direction) are discussed.

2 Computational Strategies

Two approaches for the unsteady aerodynamic computations of an isolated CROR operating at high-speed conditions ($M_\infty = 0.73$, $alt = 10,668$ m (35,000 ft)) at angle of attack of 1 deg are presented, both solving the unsteady Reynolds-averaged Navier–Stokes equations.

2.1 CFD Solvers. The first CFD solver used for the computations is the *elsA* [23] code, which solves the compressible RANS equations on multiblock structured grids using a finite volume method. The *elsA* code has been developed by ONERA since 1997 and codeveloped by CERFACS since 2001. It has been extensively used for turbomachinery, helicopter, and aircraft applications and is the production code of several aeronautical companies (Safran, Airbus, Eurocopter, etc.).

The second CFD solver used for the computations is the *ENSOLV* code [24,25]. *ENSOLV* uses a finite volume formulation and multiblock boundary-conforming structured grids. The *ENSOLV* code was developed since 1988 as a collaboration between NLR, CIRA, and ALENIA. The code has been used for aircraft, helicopter, launcher, ship, and turbomachinery applications as well as acoustic wave propagation problems.

2.2 Numerical Setup. For the *elsA* computations, a centered Jameson scheme [26] with artificial viscosity is used for the spatial discretization. The time integration of the governing equations is based on a dual time stepping (DTS) [27] approach. The scheme for the physical time is a second-order Gear scheme, and the one

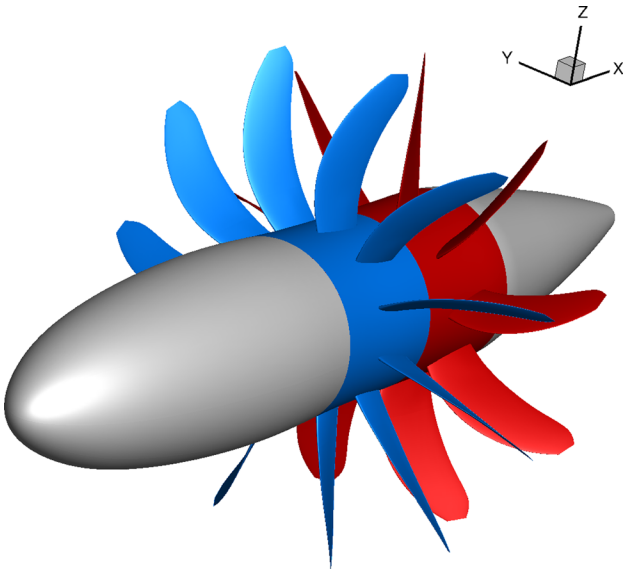

Fig. 1 AI-PX7 geometry

Table 1 AI-PX7 key parameters

Geometrical parameters	Value
Blade number ($B_F \times B_R$)	11×9
Front rotor diameter, D (m)	4.2672
Rear rotor cropping (%)	10
Rotor-rotor spacing, s (m)	0.95
Performances parameters at high-speed	**Value**
Freestream Mach number, M_∞	0.73
Front rotor rotation speed, Ω_F (rpm)	−795
Rear rotor rotation speed, Ω_R (rpm)	795
Advance ratio, J	3.83
Angle of attack, α	1 deg

for the fictive time is a first-order backward Euler scheme. The Spalart–Allmaras one-equation turbulence model [28] is used for closure of the RANS equations. A time step convergence study was performed by comparing results obtained with time steps of 0.25 deg and 0.5 deg and showed that the in-plane forces modulus and angle results present discrepancies lower than 0.1%. Thus, the simulations are performed with a time step equivalent to a propeller rotation of 0.5 deg. For the prediction of in-plane forces, the computation is considered converged when the moving average and the root mean square (rms) rotor forces vary respectively by less than 0.1% and 1% during two consecutive rotations. To fulfill this criterion, six rotations are performed. For the DTS scheme inner loop, ten subiterations are used and enable us to reach the convergence of the aerodynamic forces, as simulations with 30 subiterations show identical forces. For the implicit scheme, the lower upper symmetric successive over relation (LUSSOR) scheme developed by Yoon and Jameson is used [29]. The computations are initialized with a uniform flow-field.

For the *ENSOLV* computations, the flow equations are solved using cell-centered finite-volume schemes. The time integration of the governing equations is based on a DTS [27] approach. The scheme for the physical time is a second-order Gear scheme, and the one for the fictive time is a first-order backward Euler scheme. Kok's k-ω model [24] is used for the turbulence closure. For the current application, a fourth-order accurate finite volume scheme [25] is used. This scheme is dispersion-relation and symmetry preserving, resulting in low numerical dispersion and dissipation. This property ensures the accurate capturing of propeller slipstreams, propeller tip vortices, and acoustic waves. The convergence is reached when the thrust blade force from two consecutive rotations match. Thus, five rotor rotations are performed with 40 subiterations (simulations with 60 subiterations present identical forces). The simulations are performed with a time step equivalent to a propeller rotation of 0.5 deg. For the implicit scheme, the implicit residual averaging developed by Jameson and Yoon [30] is used. The computations are initialized with a uniform flow field.

2.3 Computational Domain and Boundary Conditions. Unsteady simulations of propellers at nonzero angles of attack require the use of a full annulus computational domain. No periodicity can be established between flow features of neighboring blades because each blade has a different inflow depending on its azimuthal position. The computational domain is bounded by a cylindrical box.

For *elsA* computations, its dimensions are 28 times the radius of the front rotor in the axial direction and 13 times the radius of the front rotor in the radial direction. The external boundaries are modeled with a nonreflective condition, which prevents the acoustic waves from reflecting on the external boundaries. The methodology is based on a characteristic relation approach using a gradient technique for the determination of the wave propagation direction (see Couaillier [31]). All the walls (blades and nacelle) are modeled with an adiabatic condition of viscous wall.

For *ENSOLV* computations, the dimensions of the computational domain are 14 times the radius of the front rotor in the axial direction and four times the radius of the front rotor in the radial direction. At the external boundaries, the freestream state vector is imposed. Large cells neighboring the external boundaries enable damping of the reflection of acoustic waves. Walls on blades are modeled with an adiabatic condition of viscous wall while the nacelle is modeled with wall slip condition.

The dimensions of the computational domain for both codes are consistent with the standards reported in the literature for CROR simulations [15,16,32]: (i) a radial length of the computational domain of at least three times the rotor diameter and (ii) an axial extent of at least seven to eight diameters.

3 Open Rotor Test Case

The open rotor test case is the AI-PX7 configuration, pictured in Fig. 1. This is a generic open rotor designed by Airbus [33] and used to test, validate, and develop numerical approaches, within the Clean Sky JTI-SFWA European project in terms of CFD techniques and mesh requirements, and enhance the understanding of the complex aerodynamics around CROR. The geometry is an 11×9 bladed pusher configuration with a rotor diameter of $D = 4.2672$ m (14 ft). Inlet and exhaust are not modeled in the nacelle shape. Table 1 gives a short overview of the AI-PX7 configuration features in high-speed conditions.

The blade geometry used in this paper is a blade with a sweep function varying from negative value at low radius to positive values up to the tip, as shown in Fig. 4. The transonic blades need to be swept to decrease the magnitude of the shock structure. The blade has a low thickness-to-chord ratio, similar to current transonic fan blades, and low camber throughout its span. The rear rotor diameter is reduced by 10% relative to the front blade while the rear blade chord is increased in order to generate a thrust of equivalent magnitude for both rotors. The rear rotor cropping enables us to decrease the impact of tip vortices convected from the front rotor to the rear rotor.

The nacelle design corresponds to a transonic nacelle design with the objective of minimizing as much as possible the local Mach number seen by the blades. The flow is, thus, only slightly accelerated by the front part of the nacelle. In high-speed conditions, Mach number increases from 0.73 in the freestream to 0.75 just upstream of the front rotor. The nacelle designs used in *elsA* and *ENSOLV* simulations for the comparison are slightly different (see Fig. 2). Considering that the maximum cross section of both

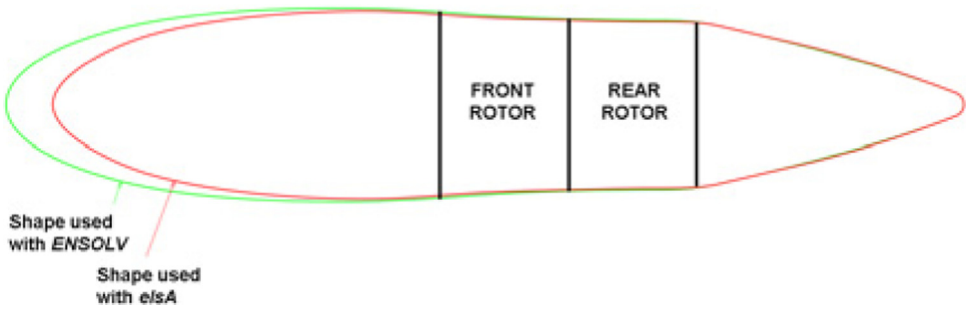

Fig. 2 Two different Airbus nacelle designs for AI-PX7 configuration

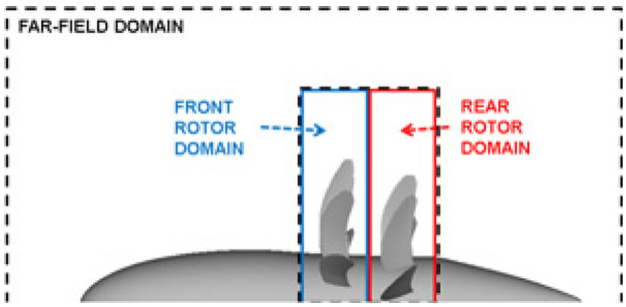

Fig. 3 Splitting of the computational domain

nacelles are very close and drive the acceleration of the incoming flow, it is assumed that these geometrical differences have a negligible impact on the in-plane forces.

4 Open Rotor Meshing

An open rotor configuration is composed of fixed parts (front and rear parts of the nacelle) and rotating parts (front rotor) and contra-rotating parts (rear rotor). This leads to a split of the mesh into three distinct domains: one far-field fixed mesh and two cylindrical rotating meshes (one for each rotor), pictured in Fig. 3. Each rotor mesh is contained in a cylindrical domain. This enables us to refine the mesh around the blade areas without any propagation of refined mesh into the far-field area. This mesh strategy is also suitable for the modeling of installation effects on aircraft.

4.1 Grid Density. For *elsA* computations, the whole mesh contains around 53×10^6 nodes. The far-field mesh contains 5×10^6 nodes. The front and rear rotor meshes contain 26.5 and 21.5×10^6 nodes, respectively. The periodicity in each rotor is fully exploited for the mesh. Each rotor can be split into channels. For each channel, the blade is meshed by a C-block. H-blocks surround the C-block to complete the channel. The front blade contains 69 points on the chord direction and 86 points in the spanwise direction (see Fig. 4). The rear blade contains 113 points on the chord direction and 82 points in the spanwise direction. The blade-to-blade passage contains 75 points in the azimuthal direction (see Fig. 5). The axial mesh density is higher on the rear blade in order to capture unsteady wake effects from the front blade. To capture accurately the boundary layer on the blades and nacelle, 25 points are used, with a y^+ around one in the first cell.

For the *ENSOLV* computations, the whole mesh contains around 3.7×10^6 nodes. The far-field mesh contains 1.7×10^6 nodes. The front and rear rotor meshes contain 1.1 and 0.9×10^6 nodes, respectively. The blade surface resolution is 40 cells in the chord direction

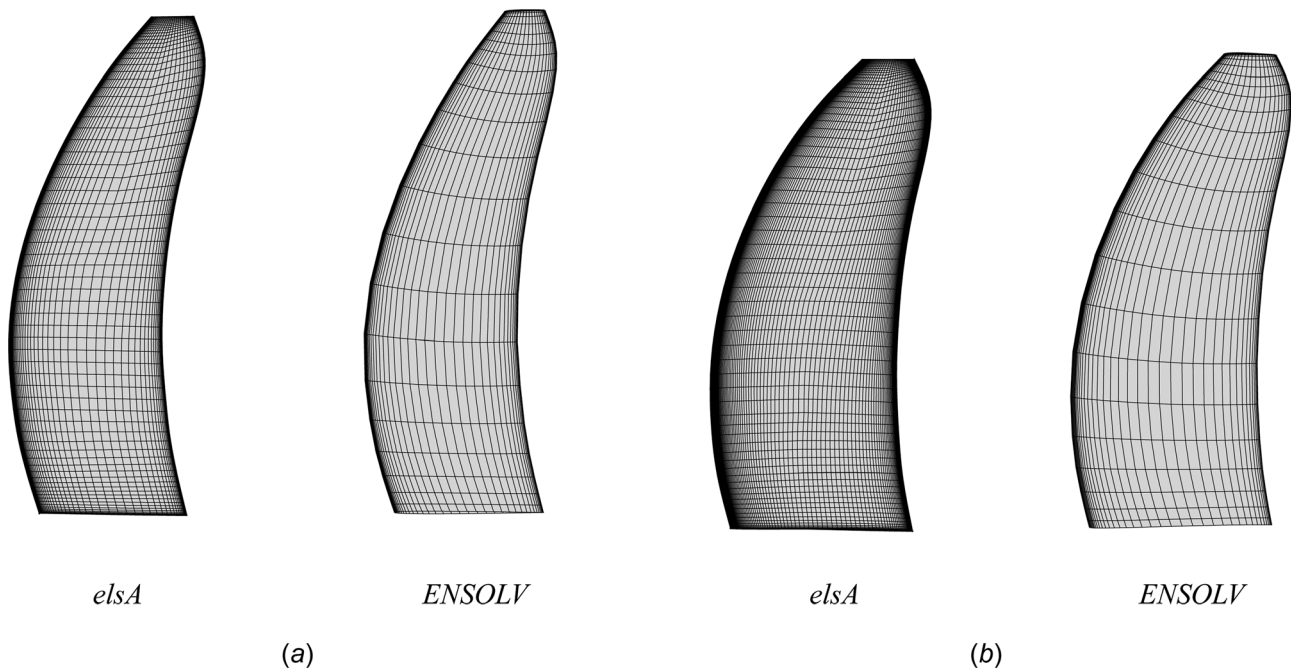

Fig. 4 Blade mesh: (*a*) front blade and (*b*) rear blade

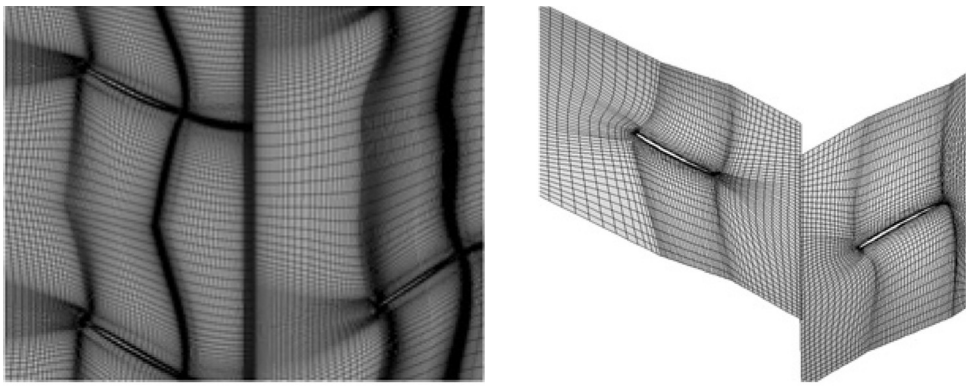

(*a*) (*b*)

Fig. 5 Blade to blade mesh: (*a*) *elsA* and (*b*) *ENSOLV*

Table 2 Comparison of grid densities

		Grid density (number of points)		Density ratio $\frac{elsA}{ENSOLV}$
		elsA	*ENSOLV*	
Computational domain	Far-field	5*M*	1.7*M*	1.42^3
	Front rotor	26.5*M*	1.1*M*	2.85^3
	Rear rotor	21.5*M*	0.9*M*	2.85^3
Front rotor	Blade chord	69	40	1.72
	Blade-to-blade azimuth	75	48	1.56
	Blade span wise	86	22	3.90
Rear rotor	Blade chord	113	40	2.82
	Blade-to-blade azimuth	75	48	1.56
	Blade span wise	82	22	3.72
Boundary layer		25	16	1.56

and 22 cells in the spanwise one. The blade-to-blade passage contains 48 points in the azimuthal direction. For the blade topology, one row of O-blocks surrounds the blade. To capture accurately the boundary layer on blades, 16 points are used, with a y^+ around two in the first cell. This is followed by H blocks to fill up the channel.

Grid density features of both meshes are gathered in Table 2. Table 2 also highlights the ratio of density between the two meshes. The mesh density ratio is defined as the ratio between the number of nodes in *elsA* and *ENSOLV* for a domain (front, rear, far-field)[2] or a specific direction (chord, span). Larger discrepancies are observed in the spanwise direction, in which the *elsA* mesh is about four times more refined. This is partly due to the nonmodeling of the boundary layer of the nacelle with the NLR mesh. Mesh size discrepancies in the chord and azimuthal directions for blades are more moderate with a ratio of around 1.6. These grid densities were chosen for each code with regard to their best practices and their numerical setup, especially with respect to the order of the spatial numerical schemes used.

4.2 Sliding Mesh Technique. Unsteady full annulus computations of open rotors rely on moving grid techniques. To achieve this, the sliding mesh technique is used for both computations. The sliding mesh technique is based on the use of nonconforming grid systems having different relative motions. A sliding surface can be defined as the boundary between two nonconformed meshes. Nonconforming meshes have been first used with fixed meshes in order to optimize the size of structured mesh [34] and ease the generation of meshes for complex geometry [35]. This technique has been extended to grids with different relative motions. A recent industrial application was the aerodynamic simulation of a multistage compressor [36]. However, sliding mesh implementations differ for *elsA* and *ENSOLV* codes and are detailed below.

In *elsA*, the communication through the sliding surface is performed using a distribution of fluxes through the nonmatching interfaces, which rigorously ensures conservativity for planar interfaces. More details on the implementation and use of the sliding mesh technique with the *elsA* code can be found in the work of Fillola et al. [35] and Gourdain et al. [36].

In *ENSOLV*, the fluxes are computed using the flow states in one row of dummy cells. The flow states in the dummy cells are interpolated using bilinear interpolation techniques. The interpolation coefficients are based on the cell face center coordinates on each side of the sliding interface. A recent application of the sliding mesh technique with the *ENSOLV* code can be found in Laban et al. [19].

5 Comparison and Analysis of Results

This section presents the results of the *elsA* and *ENSOLV* simulations. Rotor forces, blade forces, and pressure distributions over different azimuths are compared. Forces on the nacelle are not considered here because this nacelle is a simple design used for test and validation of aerodynamic methods and is not representative of a nacelle used for flight (no air intake or outlet). Thus, only forces on the blades will be analyzed. The reference axes and angles used in this paper are shown in Fig. 6. Azimuthal angles $\theta_{F,R}$ will be counted positively in the rotation direction.

5.1 Rotor Forces

5.1.1 Definitions. First, the forces applied on a whole rotor stage are analyzed and compared. The global forces are obtained

[2]The mesh density ratio is here expressed to the third power to give an average density ratio for each direction.

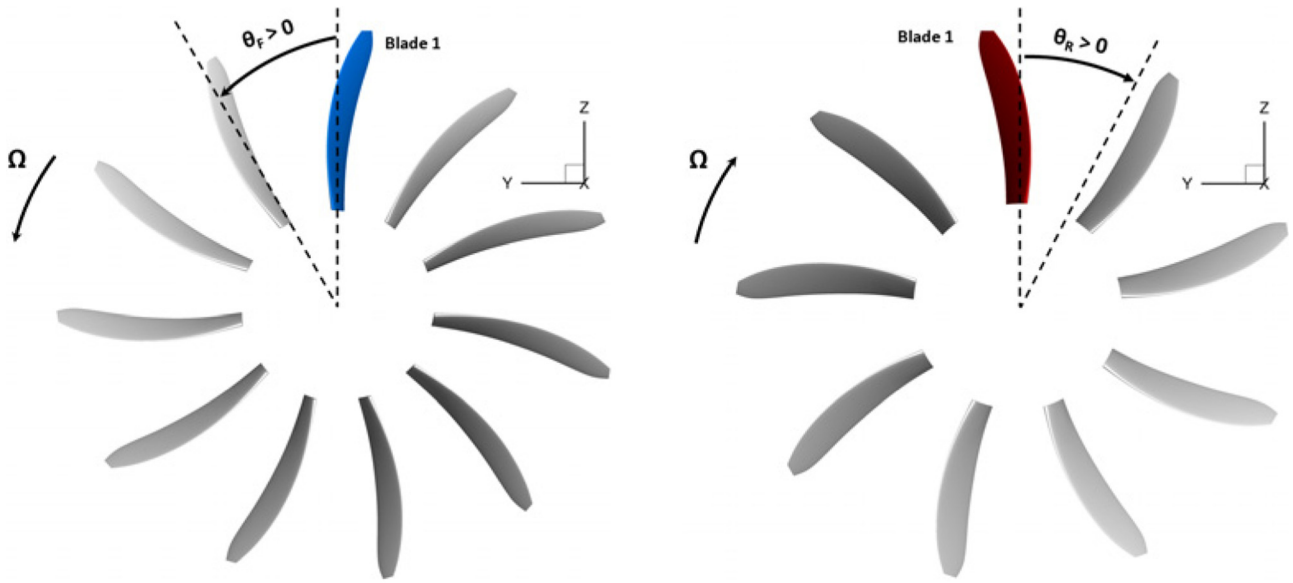

(*a*) (*b*)

Fig. 6 Definition of the azimuthal angle: (*a*) front rotor and (*b*) rear rotor

by summing up all the contributions of the blades for each rotor. Rotor forces are split into the component along the rotation axis, commonly called thrust, and the component in the propellers plane called in-plane forces (here, YZ-plane). In-plane forces can then be decomposed with projection on the reference axis in which vertical and side components are used. This decomposition of the in-plane forces is commonly found in many works in the literature [12,13,21] because the projection on the aircraft axis is straightforward. However, a modulus/angle decomposition (F_{IP}, ψ_{IP}) is preferred in this work because aerodynamic mechanisms behind each term can be separated. Modulus F_{IP} and angle ψ_{IP} are then defined as follows:

$$F_{IP} = \sqrt{F_Y^2 + F_Z^2}, \quad \psi_{IP} = \arctan\left(\frac{F_Y}{F_Z}\right) \tag{1}$$

By convention, ψ_{IP} is oriented in the rotation direction for each rotor stage. Nondimensional thrust C_T and in-plane force modulus C_{IP} are used.

$$C_T = \frac{T}{\rho_\infty n^2 D^4}, \quad C_{IP} = \frac{F_{IP}}{\rho_\infty n^2 D^4} \tag{2}$$

5.1.2 Comparison. Figure 7 presents thrust, nondimensional in-plane forces modulus C_{IP}, and angle ψ_{IP} for each rotor stage (only blades are accounted for). The rotor thrust shows an almost-steady signal over a rotation. Fluctuations are negligible for the front stage and very low for the rear blade (magnitude is around 0.1% relatively to the mean value). Mean thrust mismatches between *elsA* and *ENSOLV* results are very small (<1% for the front rotor and <0.3% for the rear rotor).

The C_{IP} signal describes a periodic evolution with a peak-to-peak fluctuation lower than 1% for the front rotor and around 6% for the rear rotor. These fluctuations are due to the aerodynamic interactions between rows. A mean C_{IP} mismatch between *elsA* and *ENSOLV* simulations is observed on the front rotor (discrepancies around 2%) while it matches well on the rear rotor. Correlations between codes are observed as well on the mean angle ψ_{IP} for the front rotor (0.5 deg) and for the rear rotor (1 deg). The same magnitude of fluctuations due to the aerodynamic interactions is captured by both codes (0.5 deg for the front rotor and 3 deg for the rear rotor).

To conclude, this comparison shows consistent results for both codes on rotor forces.

5.1.3 Fourier Analysis. A fast Fourier transform (FFT) is applied on the C_{IP} signal for both rotors over four complete rotations in the absolute frame and presented in Fig. 8. Given the time step used, frequencies above $40n$ are not considered here since they are not sampled accurately (less than 18 points in the period). According to the framework proposed by Tyler and Sofrin [37], rotor/rotor interactions give rise to frequencies characterized in the absolute frame of reference by $h_F B_F n + h_R B_R n$, where h_F and h_R are relative integers, B is the blade number, and n is the rotation speed. For both rotors, a major peak arises at a frequency of $20n$ ($h_F = 1, h_R = 1$). The front rotor FFT presents secondary peaks of one of order of magnitude less than the major peak for frequencies of $2n$ (1,–1), $9n$ (0,1), and $11n$ (1,0). The rear rotor FFT shows secondary peaks for frequencies $1n$ (5,–6), $9n$ (0,1). The frequency of $1n$ is unexpected because the harmonics involved are high. This frequency may be nonphysical and due to a lack of convergence.

The peak magnitudes for the rear rotor spectrum are approximately one order of magnitude higher than the ones from the front rotor. This highlights that the wakes play a major role in the aerodynamic interactions.

5.2 Blade Thrust. The comparison now focuses on the local thrust of one blade, which is key data to understand and validate in-plane forces predictions. Figure 9 compares the thrust level of one blade (from each rotor) over one rotation for both computations at an angle of attack of 1 deg. The thrust level for $\alpha = 0$ deg is also shown to highlight the effect of a nonzero angle of attack. The blade thrust signal emphasizes two aerodynamic phenomena with widely separated frequencies: the aerodynamic interactions and the effect of a nonzero angle of attack. This latter effect is characterized by a frequency equal to the frequency of rotation while aerodynamic interactions frequency, in the relative frame of reference, are the blade passing frequencies (BPF_F, BPF_R). The variation of the thrust due to the effect of a nonzero angle of attack over one rotation is very important with regard to the mean thrust compared to the variations simulated with a zero angle of

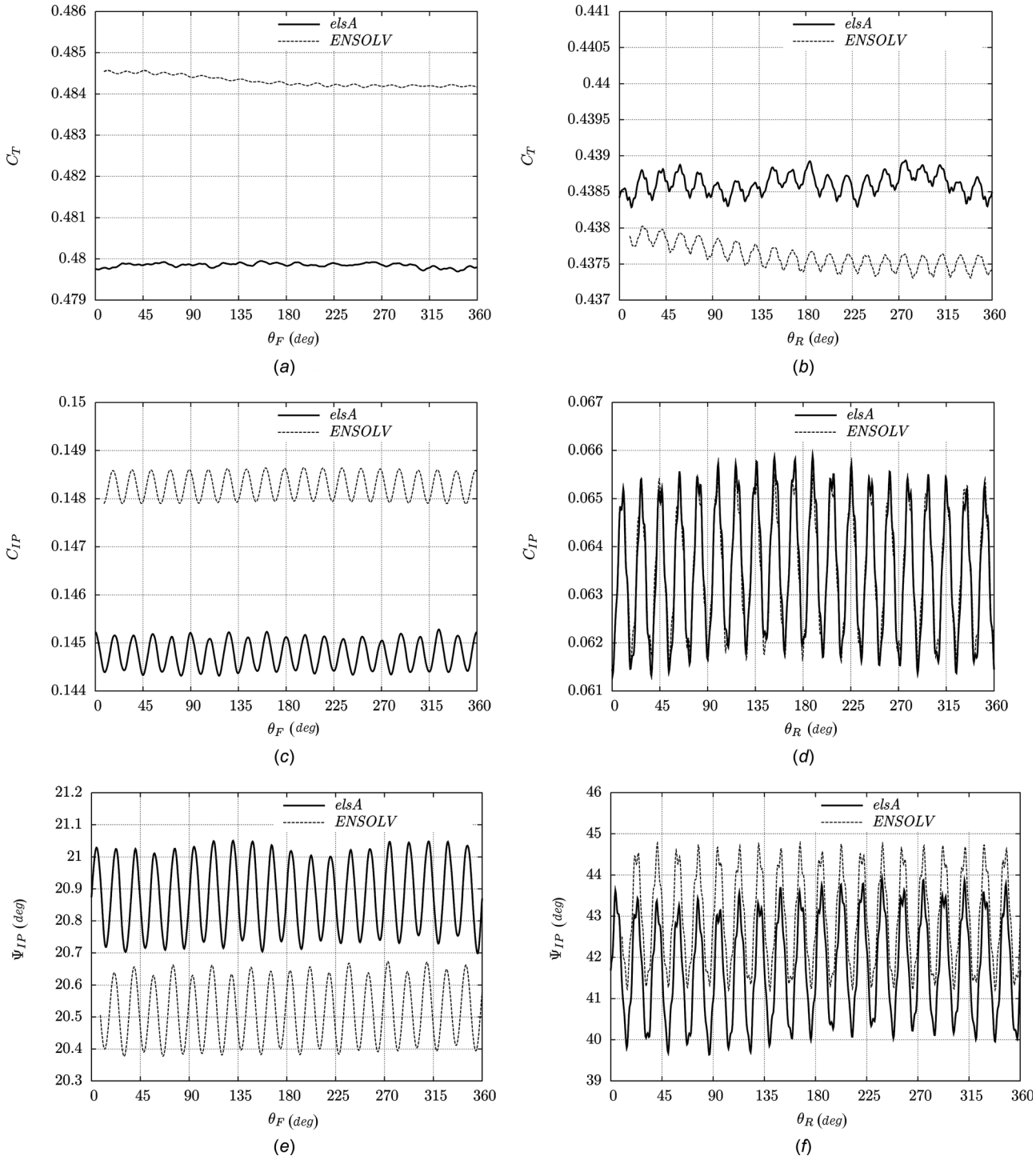

Fig. 7 Global forces on rotors: (*a*) thrust coefficient on the front rotor, (*b*) thrust coefficient on the rear rotor, (*c*) in-plane force modulus on the front rotor, (*d*) in-plane force modulus on the rear rotor, (*e*) in-plane force angle on the front rotor, and (*f*) in-plane force angle on the rear rotor

attack (Fig. 9). The peak-to-peak thrust variation represents about 60% of the mean value for the front blade whereas it represents 30% for the rear blade. Fluctuations due to the aerodynamic interactions seem to vary depending on the blade loading.

Figure 9 also highlights the good matching for both computations. The effect of a nonzero angle of attack can be observed as the overall shift of the polar towards the (90 deg, 180 deg) quadrant, and aerodynamic interactions manifest as high frequency oscillations on the curve. Discrepancies appear for the maximum blade loading, in which the thrust level is slightly higher with *ENSOLV* than *elsA* on the front blade and slightly lower for the rear blade. Both codes predict a maximum thrust value for each rotor at $\theta_F \approx 120$ deg for the front blade and $\theta_R \approx 135$ deg for the rear blade.

5.3 K_p Distributions. The pressure distributions are compared to verify the local behavior of the flow at specific radii. The nondimensional pressure coefficient K_p specific to propellers is used and defined as follows:

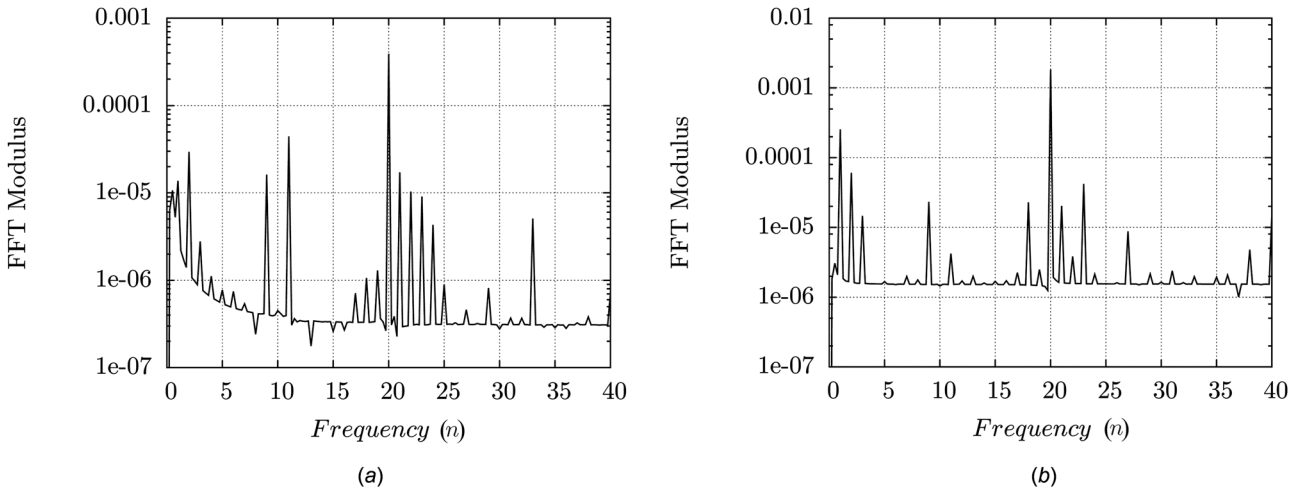

Fig. 8 Fast Fourier transform on C_{IP} signal from *elsA* computations: (*a*) front rotor and (*b*) rear rotor

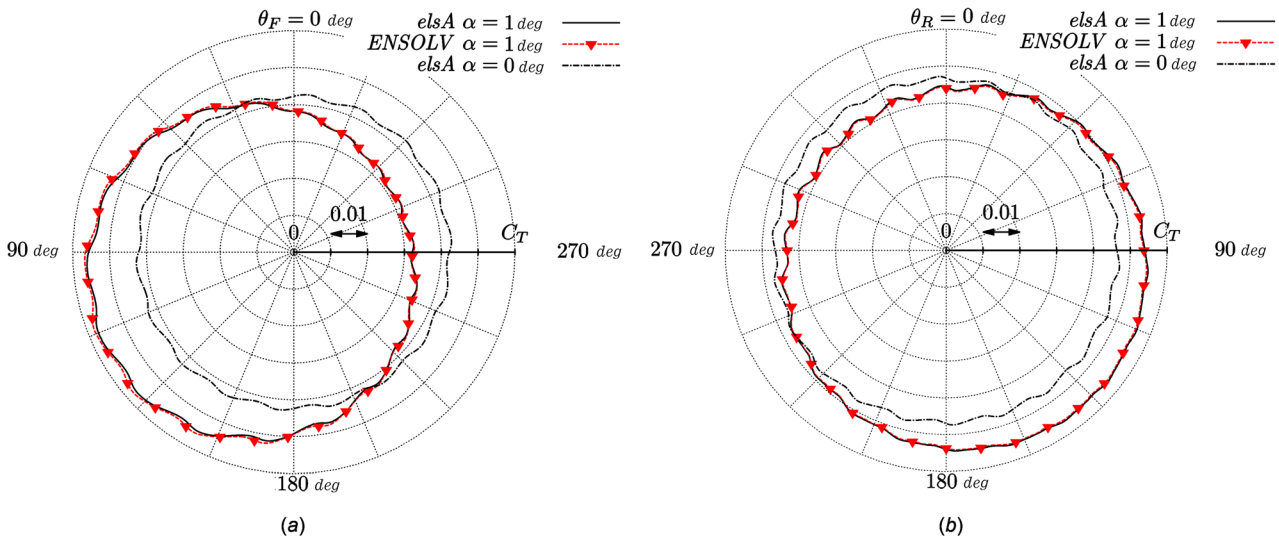

Fig. 9 Thrust coefficient C_T on a single blade: (*a*) front blade and (*b*) rear blade

$$K_p = \frac{p - p_\infty}{\frac{1}{2}\rho_\infty (V_\infty^2 + (r\Omega)^2)} \tag{3}$$

Figure 10 presents a comparison of the K_p distributions for the radius ($\xi = r/R = 0.75$). This radius was chosen because the blade develops the main part of its thrust in the area from $\xi = 0.70$ to the tip, and this section is often analyzed in literature. The aim is to observe how both codes capture the local flow physics around the blades. Various azimuthal positions are shown here.

Figure 10 presents good correlations between the *elsA* and *ENSOLV* results. In Fig. 10, small differences appear mostly on the suction side where the pressure is rising ($-K_p$ decreases), in particular in the last quarter of the chord where a shock structure is visible.

5.4 Discussion. The comparison of several key aerodynamic flow features from two computations performed with two different codes (*elsA*, *ENSOLV*), on two different meshes (grid density, size of the computational domain), with two different numerical settings (turbulence model, spatial scheme, far-field, and nacelle boundary conditions) shows very consistent results for the global integrated forces. Locally, only minor discrepancies are observed, such as the shock highlighted by K_p distributions analysis (see Fig. 10), and they remain sufficiently low not to modify the global forces. This good match also suggests that the boundary layer on the nacelle has a limited impact on the global forces.

Table 3 gathers the global forces averaged over a full rotation for both solvers. The influence of the grid density with the *elsA* code is also presented. For the *ENSOLV* code, the study on the grid density for open rotors simulations has already been performed but on a different case. This previous study has shown that doubling the grid density in the three directions modifies by less than 1% the global forces as compared to the current grid density used here. For the *elsA*, comparisons with a coarser grid (one point over two in each direction for the Euler mesh, 25 nodes are kept to ensure $y^+ = 1$ on the wall, which gives a total amount of $9M$ of points) show differences on global forces compared to the current grid. Rotor thrust predicted with the coarse grid is underestimated by 3% and 5% compared to the current grid, respectively, for the front and rear stage. Oddly, in-plane force modulus difference and angle difference for the front stage are much smaller (1%) whereas the rear angle difference is around 5%. For this application, the *elsA* code requires a finer grid density than the *ENSOLV* code to reach the mesh convergence. The mesh size used with *ENSOLV* seems to be sufficient to get the global forces. The fourth-order space discretization used in *ENSOLV* contributes partly to reach the mesh convergence with fewer points compared to the *elsA* code, for which a second-order scheme is used.

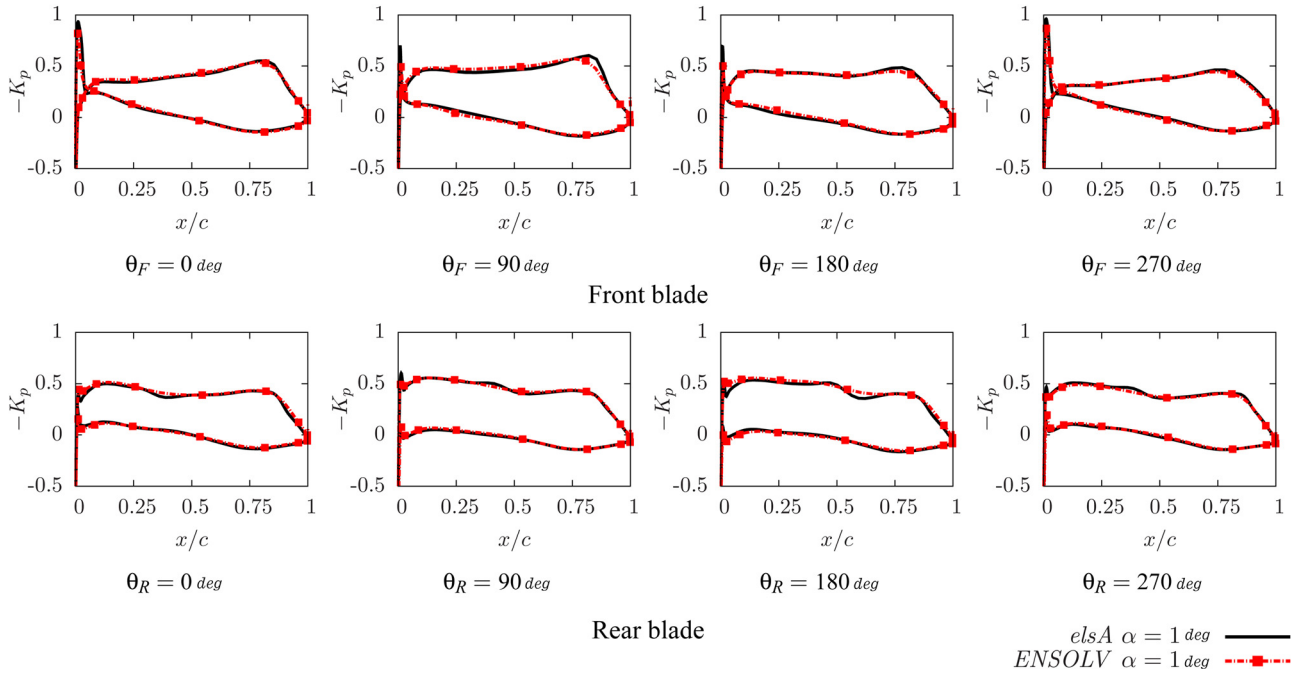

Fig. 10 K_p **distribution on blade at** $\xi = 0.75$

Table 3 Average global forces sensitivities regarding the mesh size and the turbulence model

		elsA			*ENSOLV*
Grid size		Current (53*M*)	Coarse (9*M*)		Current (3.7*M*)
Turbulence Model		SA	SA	$k-\omega$	$k-\omega$
Front rotor	$\overline{C_T}$	0.4804	0.4633	0.4676	0.4843
	$\overline{C_{IP}}$	0.1447	0.1421	0.1430	0.1482
	$\overline{\psi_{IP}}$(deg)	20.8	20.6	20.8	20.5
Rear rotor	$\overline{C_T}$	0.4392	0.4176	0.4228	0.4376
	$\overline{C_{IP}}$	0.06352	0.06369	0.06355	0.06356
	$\overline{\psi_{IP}}$(deg)	41.7	39.9	40.5	42.9

As both simulations were performed with different turbulence models, an additional simulation was performed with the *elsA* code on the coarse grid with the $k-\omega$ turbulence model to measure its impact on the in-plane forces prediction. Comparison of these results with the Spalart–Allmaras ones highlights discrepancies around 1% for the front stage. The rear stage in-plane force modulus remains quasi-unchanged while thrust coefficient and angle increase by 1% and 2%, respectively. Consequently, the influence of the turbulence model has the same order of magnitude as the discrepancies observed between the two codes.

To conclude, this comparison highlights consistent and encouraging results (the maximum discrepancies are below 2%) and is a promising step in the verification process of prediction tools. Experimental measurements would be an excellent way to consolidate the reliability of these results. Altogether, the consistency of the results builds enough confidence to perform a deeper analysis of the physics behind in-plane forces in the following section.

6 Understanding the Physics Behind In-Plane Forces

This section aims at understanding the physics behind the in-plane forces. First, an in-depth analysis of the phenomena contributing to in-plane forces applied to the front rotor is investigated. Second, the same analysis is performed on the rear stage. Based on this analysis, differences between in-plane forces from front and rear rotors are discussed. This section presents only the results performed with the *elsA* code.

6.1 Understanding the In-Plane Force on the Front Rotor.

For the front rotor, the aerodynamic simulation on the AI-PX7 configuration at high-speed at an angle of attack of 1 deg predicts a mean in-plane force modulus of 30.0% with respect to its rotor thrust and a mean angle of 20.8 deg. This section details the mechanisms contributing to the modulus and the direction of the in-plane force. First, a quick reminder of the freestream velocity effect will be given. Second, the influence of the induced velocity will be analyzed. Third, the impact of the potential effects from the opposite stage on the in-plane forces will be studied.

6.1.1 Freesrteam Velocity Effect. At zero angle of attack, the freestream velocity vector is perpendicular to the rotation plane of the propellers. With a nonzero angle of attack, its projection on the rotation plane leads to a nonzero vector and the velocity triangle is modified. The impact of the freestream velocity on the velocity diagram is called here the freestream velocity effect. Figure 11 illustrates the velocity diagram for a propeller at nonzero angle of attack. W_∞ represents the freestream velocity projected in the propeller rotating frame and is defined as follows:

$$\begin{aligned}\mathbf{W}_\infty &= \mathbf{V}_\infty - r\Omega\,\mathbf{e}_\theta \\ &= V_\infty \cos\alpha\,\mathbf{e}_\mathbf{x} + [V_\infty \sin\,\alpha\,\sin\,\theta - r\Omega]\mathbf{e}_\theta\end{aligned} \tag{4}$$

The region between $\theta_{F,R} = 0\,\text{deg}$ and $\theta_{F,R} = 180\,\text{deg}$ is called advancing blade whereas the other region is called retreating blade. In the advancing part, the angle of attack component $V_\infty \sin\alpha$ is summed up to the rotating speed and contributes to an increase of the local incidence α_{loc} (see Fig. 11). Thus, blades in the advancing part generate more lift and drag, which means, by projection, more thrust and torque about the rotational axis. An opposite effect is obtained on the retreating part by symmetry. The projection of lift and drag on the propellers plane leads to an in-plane force with a zero angle.

6.1.2 Induced Effect. The flow circulation around the blades and the nacelle modifies the velocity field in the vicinity of these

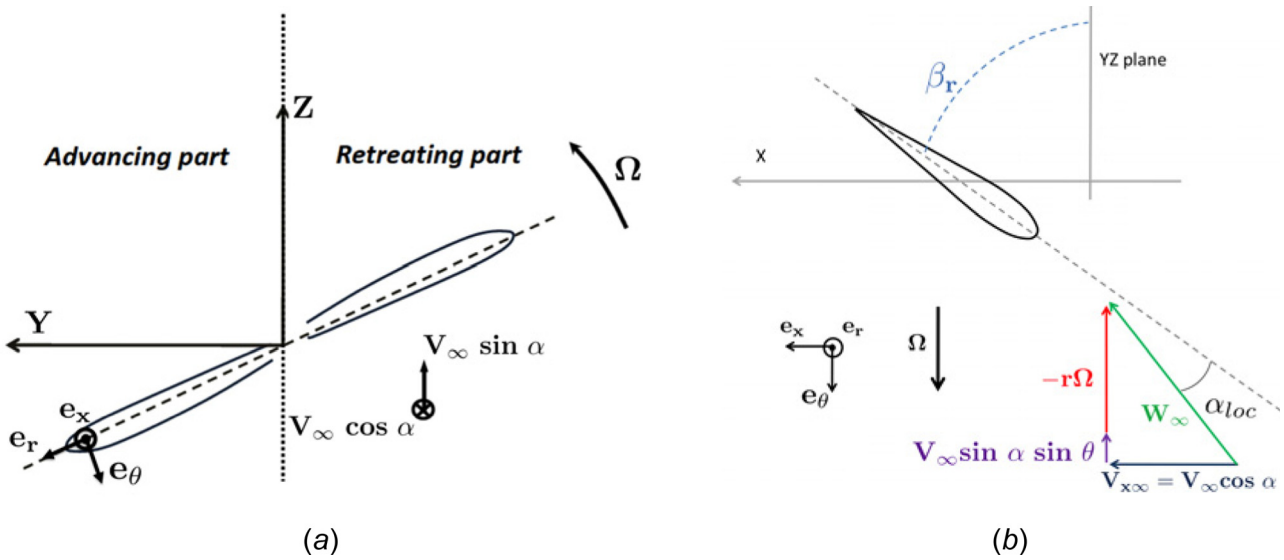

Fig. 11 Velocity triangle for propellers at nonzero angle of attack: (*a*) front view of propellers and (*b*) advancing blade

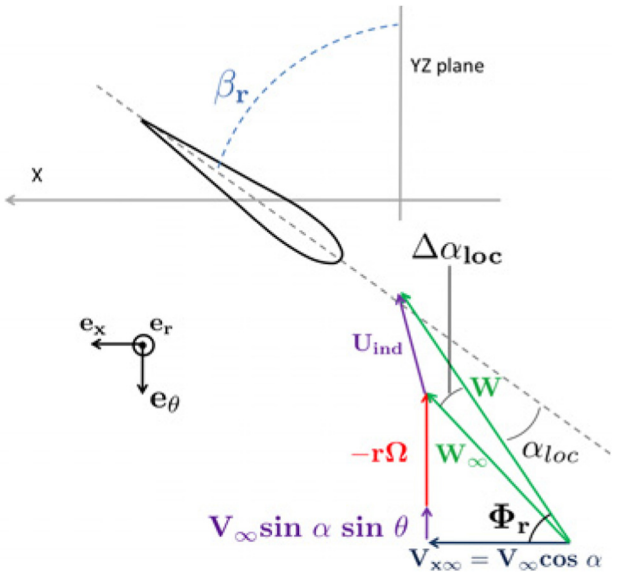

Fig. 12 Velocity triangle for propellers at nonzero angle of attack with induced velocities

areas. This phenomenon is defined as the induced effect. The flow circulation around the blades varies depending on the azimuthal position and, consequently, the analysis of the velocity triangle seen by the blade becomes much more complex than what was proposed in Fig. 11. To evaluate this impact of the induced effect, the induced velocity $\mathbf{U}_{\text{ind}}$ is defined as the difference between the velocity $\mathbf{W}$ and the freestream velocity $\mathbf{W}_\infty$ in the rotating frame as follows:

$$\begin{aligned} \mathbf{U}_{\text{ind}} &= \mathbf{W} - \mathbf{W}_\infty \\ &= u_x\,\mathbf{e_x} + u_\theta\,\mathbf{e_\theta} \end{aligned} \tag{5}$$

Figure 12 illustrates how induced velocities impact the velocity triangle. For a better understanding of the impact of the induced velocities on the flow, the variation of the local incidence $\Delta\alpha_{\text{loc}}$ is introduced and defined as the oriented angle $(\mathbf{W}_\infty, \mathbf{W})$.

Figure 13(*a*) displays the axial induced velocity field $(u_x/V_{x\infty})$ estimated from CFD simulations on an X-plane cut at one chord upstream of the front rotor. The axial induced velocity field is positive all over the disk because the front rotor generates suction. Over a rotation, induced axial velocities around the blade-to-blade passage present maxima values in the angular area from approximately $\theta_F = 30\,\text{deg}$ to $\theta_F = 120\,\text{deg}$, which is consistent with the thrust variation on a single blade as seen in Fig. 9. Blades on the advancing part generate more suction and, consequently, high axial induced velocity. Along the radial direction, axial induced velocity increases, reaching a maximum value around $r/R = 0.75$, and then decreases after. Axial induced velocities at $\theta_F = 0\,\text{deg}$ are greater than those at $\theta_F = 180\,\text{deg}$. Ortun et al. [21] show similar results with the HOST code on a single propeller.

To complete the analysis, Fig. 13(*b*) displays the change of local incidence $\Delta\alpha_{\text{loc}}$ due to the induced effects on an X-plane cut at one chord upstream of the front rotor. The positive $\Delta\alpha_{\text{loc}}$ value means that the local incidence is increased by the induced effect. Areas around $\theta_F = 0\,\text{deg}$ show a slightly lower value of $\Delta\alpha_{\text{loc}}$ than in the areas around $\theta_F = 180\,\text{deg}$. Blade aerodynamic loading is, consequently, higher for blade at $\theta_F = 180\,\text{deg}$ than for $\theta_F = 0\,\text{deg}$ and contributes to the generation of the lateral component of in-plane forces and, consequently, the in-plane force angle with the (Oz) axis. Areas of positive and negative extrema values of $\Delta\alpha_{\text{loc}}$ are centered on an axis driven by $\theta_F = 100\,\text{deg}$ and $\theta_F = 280\,\text{deg}$, respectively. The local incidence for the advancing blade is strongly reduced by the induced effects whereas the one for the retreating blades is increased but to a lesser extent. The induced effect tends to decrease the difference between the maximum and minimum loading of the blade over a rotation and, consequently, to decrease the modulus compared to the case without induced effect (see Sec. 6.1.1). The induced velocities present a nonsymmetric pattern between the z-positive half-plane and the z-negative one. Consequently, this distribution of induced velocities field contributes to get a nonzero angle ψ_{IP}.

The influence of the induced velocities can be explained in a different way with an induced sideslip analogy. The joint analysis of the induced velocity field (Fig. 13) and thrust variation of a single blade (Fig. 9) shows that the advancing half on each rotor generates more thrust and, consequently, more air suction (characterized by the axial induced velocity in Fig. 13) than the retreating part. This induces momentum ρv_y from the retreating half to the advancing half, which acts as if there was a sideslip angle. This induced lateral distortion creates a force in the lateral direction (Oy). Consequently, this lateral component gives a nonzero angle for the in-plane force.

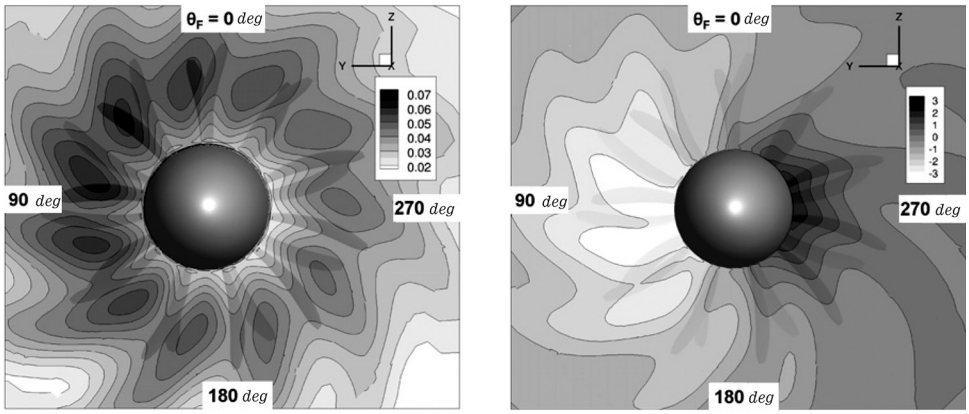

(*a*) (*b*)

Fig. 13 Instantaneous induced velocity flow-fields in an X-plane at one chord upstream of the front rotor: (*a*) normalized axial induced velocity $u_x/V_{x\infty}$ and (*b*) $\Delta\alpha_{loc}$ (deg) due to induced velocity field

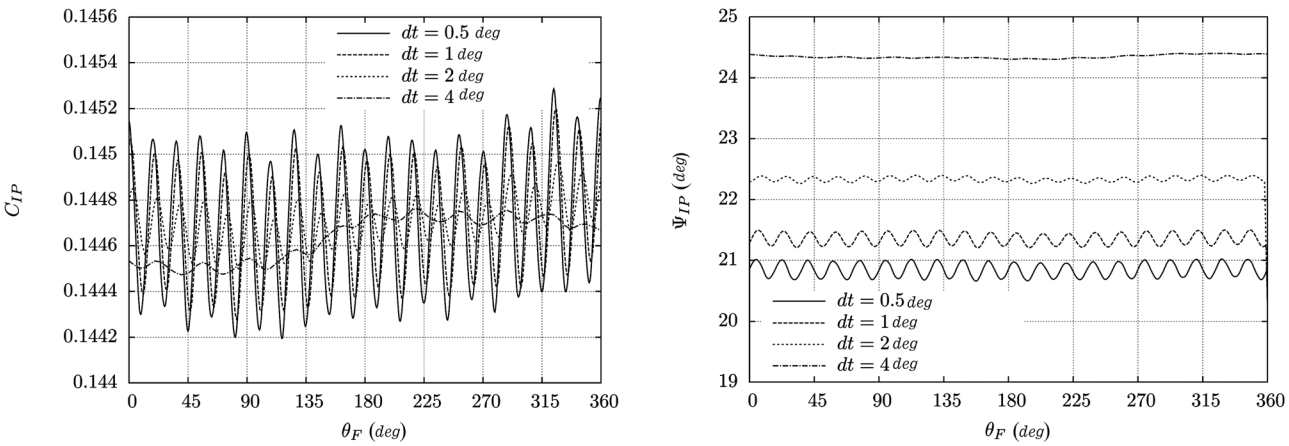

(*a*) (*b*)

Fig. 14 In-plane force on the front rotor regarding time step: (*a*) modulus and (*b*) angle

The induced effect contributes to both the angle and modulus for the in-plane force of the front rotor.

6.1.3 Impact of Aerodynamic Interactions. Potential effects from the rear rotor are seen in the front rotor frame of reference as temporal interactions characterized by the blade-passing frequency BPF_F and its harmonics. Their effect is noticeable on the thrust of a single blade as described in Sec. 5.2. A time step equivalent of 0.5 deg of rotor stage rotation enables us to sample the first harmonic of aerodynamic interactions with more than 30 points. To measure the impact of the aerodynamic interactions on the in-plane force predictions, larger time steps were used in order to degrade the capturing of these interactions and, thus, isolate their impact. Although this approach may have side-effects on the accuracy of the predictions, it provides an original way to nearly suppress aerodynamic interactions while retaining an unsteady framework suited to full annulus computation at nonzero angle of attack. Indeed, the frequency of propeller rotation, which mainly drives the effect of a nonzero angle of attack in the relative frame, is well captured for all the time steps because the largest time step used ($dt = 4$ deg) samples its period with 90 points.

Figure 14 presents the in-plane force modulus and angle for the front rotor. Variations of C_{IP} and ψ_{IP} driven by the BPF_F and its harmonics are not captured at all for $dt = 4$ deg. For $dt = 1$ deg, variations are captured but with a slightly lower magnitude than the case with $dt = 0.5$ deg but with a larger magnitude than the case with $dt = 2$ deg. Figure 14(*a*) highlights that the aerodynamic interactions do not contribute to the mean in-plane force modulus. However, the angle ψ_{IP} is more sensitive to the aerodynamic interactions. The mean angle is overestimated by, respectively, 3.5 deg with the larger time step compared to the finer one. This difference is reduced to 0.5 deg with a time step of 1deg, which remains acceptable.

In short, potential effects do not contribute to the mean in-plane force modulus but to the angle. Results with a time step of 1 deg show acceptable matching for all the variables plotted compared to the finer time step.

To understand why the in-plane force direction is more sensitive to the aerodynamic interactions, the aerodynamic behavior of the opposite stage needs to be considered. As seen in Sec. 5.2, the aerodynamic blade loading, characterized by the thrust coefficient, varies depending on its azimuthal position, which impacts the potential effects and wakes. To emphasize this coupling between the two stages, the aerodynamic loading of one single blade of each rotor is considered. Here, the impact from the rear stage to the front stage is analyzed. Thus, to quantify the aerodynamic interactions of the front blade, its thrust coefficient, expressed in the relative frame, needs to be filtered to keep only the BPF_F and its harmonics. Thus, these fluctuations can be isolated by filtering the low-frequency term linked to the frequency of rotation and

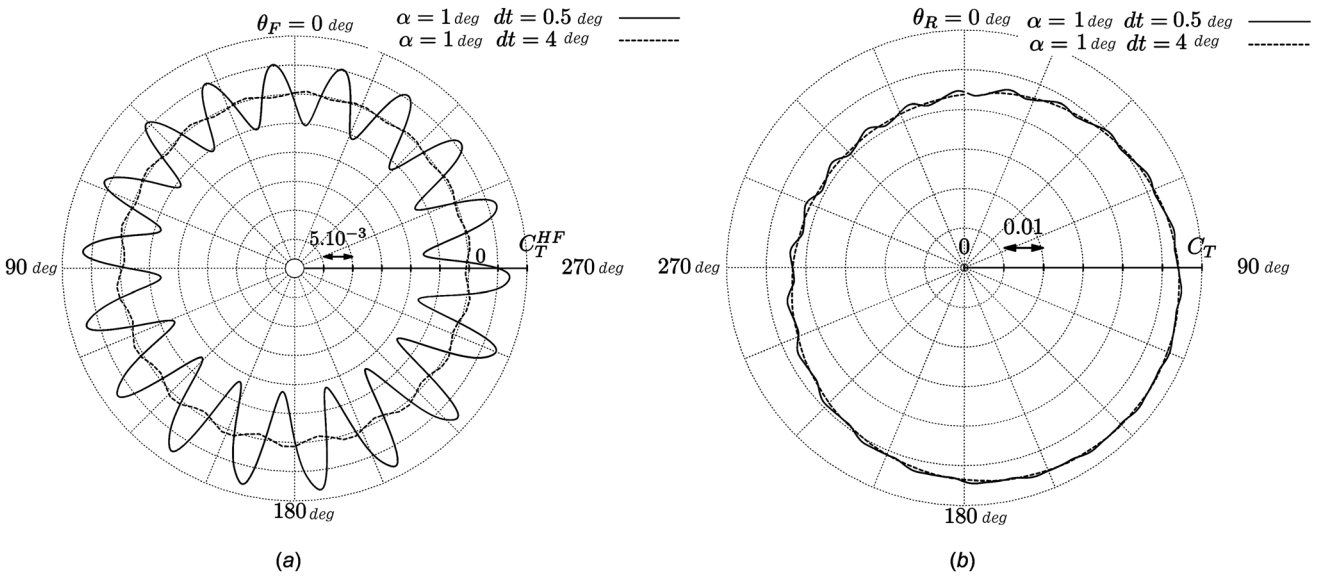

Fig. 15 Impact of the aerodynamic interactions on a front single blade: (*a*) filtered thrust coefficient C_T^{HF} on a front single blade and (*b*) thrust coefficient C_T on a rear single blade

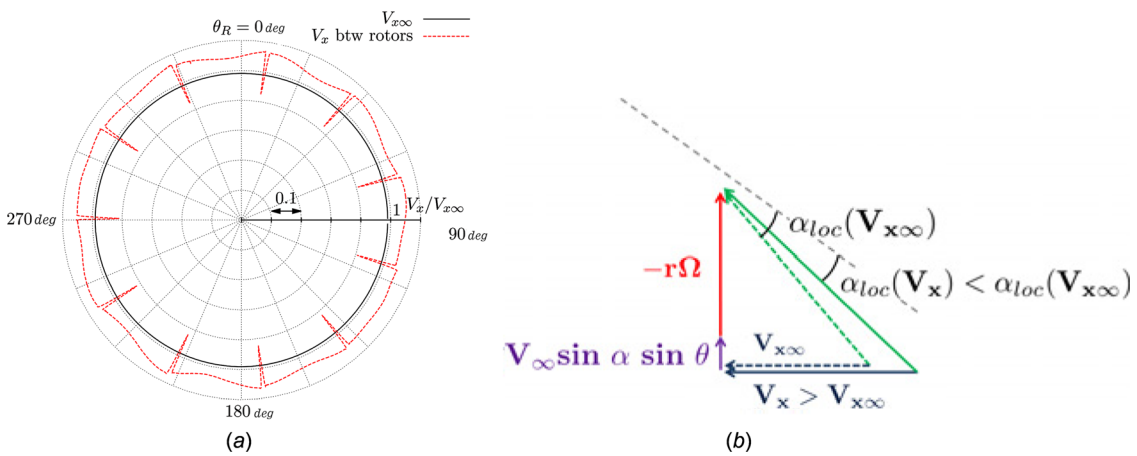

Fig. 16 Impact of the increase of the axial velocity due to the front stage: (*a*) axial velocities on an X-plane at one chord upstream to the rear rotor and at $\xi = 0.75$ and (*b*) velocity triangle for the advancing blade

subtracting the mean value on the C_T signal. The term C_T^{HF} can be introduced for measuring the impact of the aerodynamic interactions on the thrust coefficient. It gives

$$C_T^{HF} = C_T - \overline{C_T} - C_T^{LF} \tag{6}$$

The low frequency component C_T^{LF} is driven by the rotation speed of the rotor. This component can be modeled with a sinusoidal signal whose magnitude and phase are determined with a fast Fourier transform applied on the C_T signal. Figure 15(*a*) presents the filtered C_T^{HF} thrust coefficient on a front rotor single blade for two time steps ($dt = 0.5$ deg, $dt = 4$ deg) at angle of attack $\alpha = 1$ deg. First, as observed in the previous paragraph, almost no fluctuation is captured for the large time step $dt = 4$ deg, and the filtered thrust coefficient C_T^{HF} value is close to 0. Second, for $dt = 0.5$ deg, the C_T^{HF} signal can be modeled as a sinusoidal signal whose magnitude and phase vary with the azimuth. Figure 15(*b*) completes the analysis by plotting the thrust coefficient of a single blade from the opposite stage. Joint analysis of Fig. 15(*a*) and Fig. 15(*b*) highlights that the magnitudes of the aerodynamic interactions on the front blade are influenced by the aerodynamic blade loading of the rear blade. Both magnitudes of variations of C_T^{HF} and thrust coefficient value of the rear blade reach their maximum in the area between $\theta_F = 180$ deg and $\theta_F = 270$ deg (or between $\theta_R = 90$ deg and $\theta_R = 180$ deg). The energy of the upstream potential effects is linked to the aerodynamic rear blade loading and explains the coupling. These azimuthal variations due to the aerodynamic interactions also contribute to modify the direction of the in-plane force.

6.2 Understanding the In-Plane Force on the Rear Rotor.

For the rear rotor, the aerodynamic simulation on the AI-PX7 configuration at high-speed at angle of attack of 1 deg predicts a mean in-plane forces modulus of 14.4% with respect to its rotor thrust and a mean angle of 41.5 deg. The in-plane forces modulus of the rear rotor is reduced by a factor of 2.5 compared to the front rotor. The angle is also increased by 20 deg from front to rear stage. This section details the mechanisms contributing to the modulus and the direction of the in-plane forces. First, the increase of axial velocity due the front stage is studied. Second, the deflection of the flow due to the front stage is analyzed. Third, the impact of the potential effects and wakes on the in-plane forces is investigated in more depth.

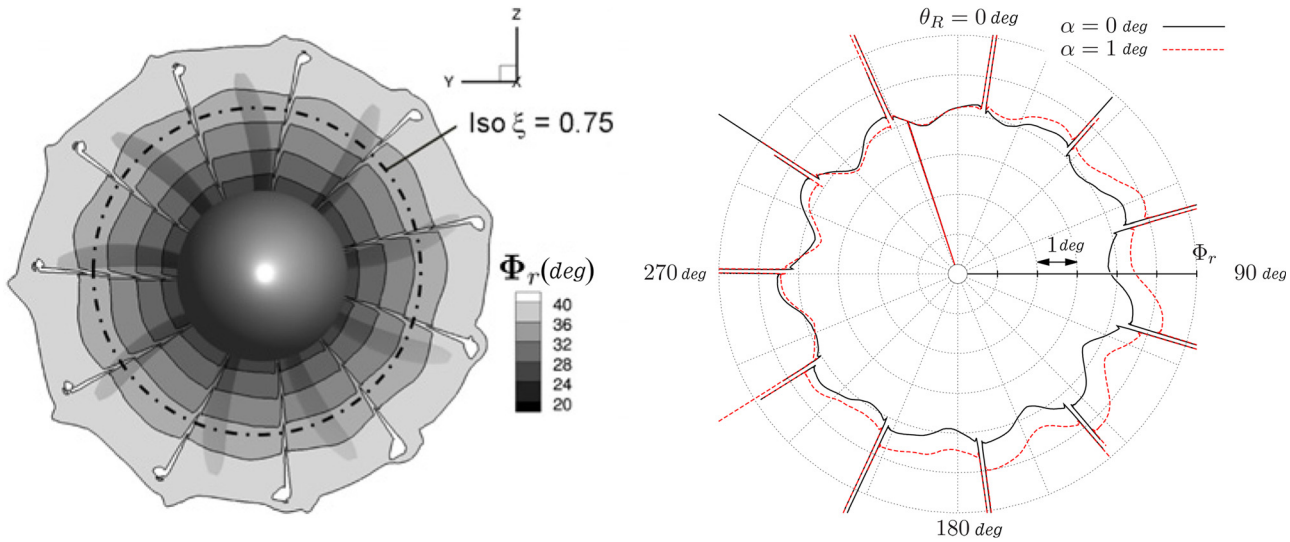

Fig. 17 Relative flow angles Φ_r (deg) upstream of the rear rotor: (*a*) X-cut at one chord upstream of rear rotor ($\alpha = 1$ deg) and (*b*) extraction from a line at $\xi = 0.75$

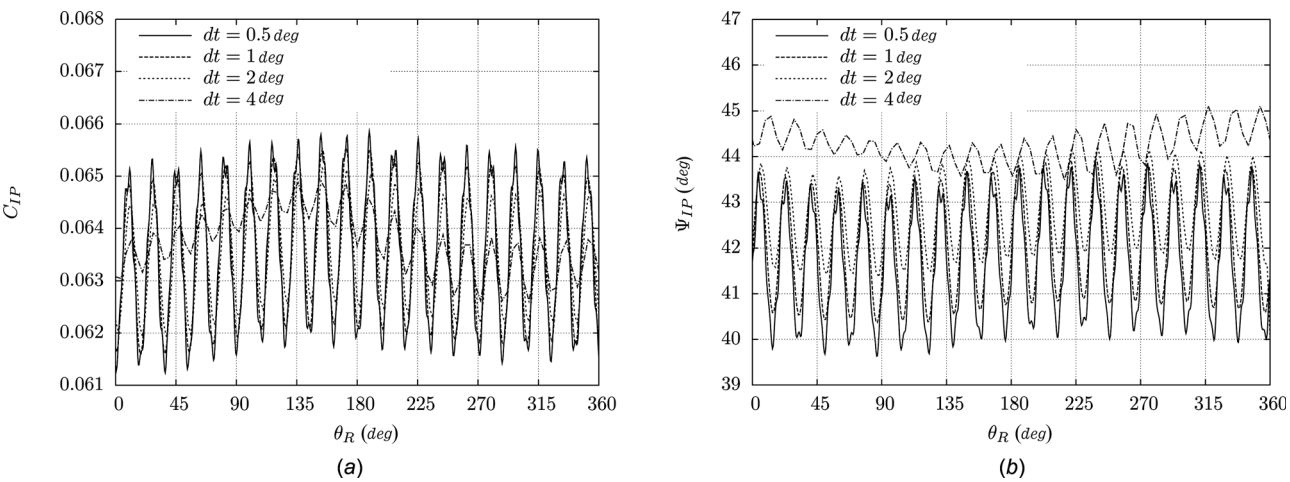

Fig. 18 In-plane forces on the rear rotor regarding time step: (*a*) modulus and (*b*) angle

6.2.1 Increase of the Axial Velocity. The front rotor generates thrust and, consequently, the axial velocity for the rear rotor is higher than the axial freestream velocity (see Fig. 16(*a*)). Consequently, the impact of the projection of the freestream velocity in the propellers plane with the term $V_\infty \sin(\alpha)$ on the velocity triangle is reduced and so is the variation of local incidence α_{loc} (see Fig. 16(*b*)). This implies a reduction of the variation of blade loading over a rotation compared to the front stage, as shown by the rear blade thrust signal in Fig. 9. The peak-to-peak magnitude of the rear signal is reduced by a factor of 2 as compared to the front one. The front rotor acts as a filter of the freestream velocity effect by decreasing its influence on the downstream rotor. Consequently, the mean increase of axial velocity contributes to decrease the in-plane force modulus.

The behavior of the propeller system is consistent with distortion processing in turbofans or multistage compressors, for which circumferential nonuniformities are reduced as the flow proceeds through the machine (see Ref. [38], for instance).

6.2.2 Swirl Effect. The deflection of the flow by the front rotor also generates an increase of the orthoradial velocity, which is called the swirl. This directly impacts the relative flow angles Φ_r seen by the rear rotor, defined as

$$\Phi_r = \arctan\left(\frac{W_\theta}{V_x}\right) \tag{7}$$

W_θ is the relative orthoradial velocity in the rear rotor rotating frame and V_x is the axial velocity. The relative flow angle Φ_r varies proportionally with the local incidence α_{loc} according to the following equation:

$$\Phi_r = \frac{\pi}{2} - \beta_r + \alpha_{\text{loc}} \tag{8}$$

Figure 17(*b*) highlights that at a constant given radius r, the relative flow angle is higher for the blades between $\theta_R = 45$ deg and $\theta_R = 215$ deg than on the opposite part. This orientation of the field of relative flow angles directly impacts the direction of the in-plane force and leads to an angle of 45 deg. This observation is fully consistent with the rear blade thrust variation observed in Fig. 9 and with the in-plane force angle in Fig. 7(*f*).

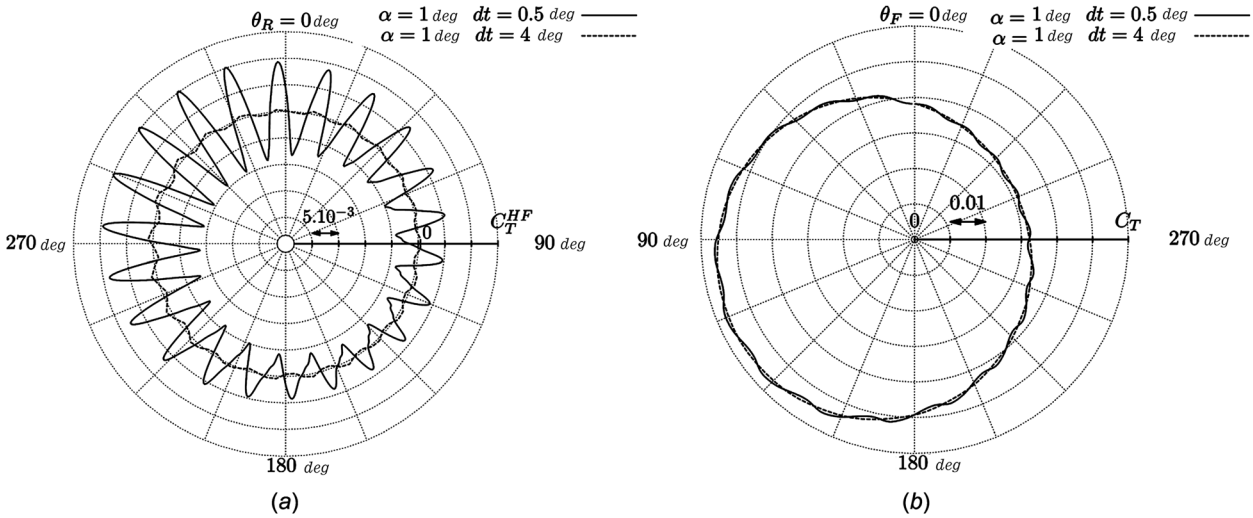

Fig. 19 Impact of the aerodynamic interactions on a rear single blade: (*a*) filtered thrust coefficient C_T^{HF} on a rear single blade and (*b*) thrust coefficient C_T on a front single blade

Figure 17 shows that the relative velocity deficit of the wakes from the front blade entails an increase of the local incidence on the rear blade, which is just the consequence of the velocity composition. Wakes impacting the rear rotor contribute to the generation of small fluctuations on the global forces on the whole rotor. The next paragraph focuses on evaluating their impact on the in-plane force component (modulus, angle).

6.2.3 Impact of the Aerodynamic Interactions. Potential effects and wakes propagating downstream from the front rotor are impacting the rear rotor and are characterized by the blade-passing frequency BPF_R and its harmonics. The same study as performed for the front rotor in Sec. 6.1.3 is applied here to the rear rotor. Figure 18 shows the in-plane forces modulus and the angle over a rotation for the rear rotor. Similar observations made in Sec. 6.1.3 apply for the rear rotor. Aerodynamic interactions do not contribute to the mean in-plane force modulus but to the mean direction. Compared to the front rotor (see Fig. 15), the variations for C_{IP} and ψ_{IP} are more important. Wakes are more energetic than potential effects and, thus, have a stronger impact.

Then, the impact of the aerodynamic interactions on a rear single blade is studied. Figure 19(*a*) presents the filtered thrust coefficient C_T^{HF} on a front single blade for two time steps ($dt = 0.5$ deg, $dt = 4$ deg) at angle of attack $\alpha = 1$ deg. C_T^{HF} was defined in Eq. (6). First, as observed in the previous paragraph, almost no fluctuation is captured for the large time step $dt = 4$ deg, and the filtered thrust coefficient C_T^{HF} value is close to 0. Second, the fluctuations of C_T^{HF} are more important than those from the front rotor as seen in Fig. 15(*a*). Figure 19(*b*) completes the analysis by plotting the thrust coefficient of a single blade from the opposite stage. Joint analysis of Figs. 19(*a*) and 19(*b*) draws similar conclusions as in Sec. 6.1.3. A correlation can be established between the magnitude of the fluctuations of C_T^{HF} for the rear rotor and the thrust distribution from the front one, but a phase-shift arises between the signals. High values of C_T are reached for $\theta_F = 120$ deg whereas high values of magnitude for C_T^{HF} are reached at $\theta_F = 45$ deg (or $\theta_R = 315$ deg). The wake released from a front blade impacts a rear blade located at a different azimuth, which may explain the phase-shift between the signals. These azimuthal variations due to the aerodynamic interactions contribute to modify the direction of the in-plane force.

7 Conclusions

In this paper, unsteady aerodynamic simulations of an isolated CROR at high-speed at a nonzero angle of attack have been compared and analyzed. Results obtained on global integrated variables such as in-plane forces and thrust show good matching between the *elsA* and *ENSOLV* codes. Mean value and fluctuations are both well captured despite different computational domain, grid densities, numerical setup, and turbulence models (the maximum discrepancies are below 2%). Analysis of pressure distribution demonstrates that local discrepancies appear in the area of shock structures but have a very low impact on the global forces. Different grid densities used on the blade skin in *elsA* and *ENSOLV* simulations probably explain these discrepancies. The comparison highlights also that an accurate prediction of global variables (thrust, in-plane forces) is reached with a coarser mesh with *ENSOLV* (3.7*M* of points) compared to the mesh used for *elsA* simulations (53*M* of points) due to a smaller computational domain, the nonmodeling of the boundary layer on the nacelle, and a higher order space scheme. Simulations with coarser mesh (9*M* of points) were performed with *elsA* and present discrepancies on the global variables. Two turbulence models (Spalart–Allmaras, $k-\omega$) were also tested with *elsA*, and their influence on the global variables appears to have the same order of magnitude as the discrepancies observed between the two codes. To conclude, the code-to-code comparison enables us to strengthen the confidence in the numerical results, which is a first step in the verification process of in-plane forces prediction.

In the second part of this work, the physics behind in-plane forces was analyzed for both rotors separately. For the front rotor, the first key mechanism is the orientation of the freestream velocity that generates different local incidences seen by the blades at different azimuths (freestream velocity effect). The second key mechanism is driven by the induced velocities, the magnitude, and the direction of which vary with the azimuth (induced effect). Both effects contribute to the modulus of the in-plane force, but only the induced effect is responsible for a nonzero in-plane force angle ψ_{IP}. To a lesser extent, aerodynamic interactions have a weak impact on the mean direction (few degrees) but no effect on its mean modulus. This contribution is explained by the nonhomogeneous impact of the aerodynamic interactions regarding the azimuthal position because potential effects energy depends on the aerodynamic rear blade loading. The physics behind rear rotor in-plane forces is more complex. The freestream velocity effect is still a major contributor to the in-plane forces but with a lesser magnitude compared to the front rotor. The front rotor behaves as a filter by increasing the mean axial velocities, which contributes to a decrease of the modulus. The second key mechanism is the swirl created by the front rotor that modifies the local incidence

seen by the rear blades, which increases the angle ψ_{IP}. Wake convection, in addition to potential effects, decrease the mean angle by a few degrees but do not affect the mean modulus. Wakes energy depends also on the aerodynamic front blade loading and their impact on the rear blades vary depending on its azimuth location.

This work offers a better validation and understanding of the in-plane forces for an isolated open rotor and can be extended to more complex applications for which in-plane forces play an important role such as whirl flutter and installed configurations applications.

Acknowledgment

This work is funded by Airbus, in the framework of CleanSky JTI-SFWA European project. The authors are particularly grateful to Airbus for permitting the publication of this paper, and wish to thank F. Blanc, R. Collercandy, F. Magaud, M. Montagnac, and C. Negulescu for their advice and help in the development of this work.

Nomenclature

B_F = number of front blades
B_R = number of rear blades
BPF_F = blade-passing frequency of the front rotor, $BPF_F = 2 \times n \times B_R$ (Hz)
BPF_R = blade-passing frequency of the rear rotor, $BPF_R = 2 \times n \times B_F$ (Hz)
C_T = thrust coefficient, $C_T = T/\rho_\infty n^2 D^4$
C_T^{HF} = high frequency component of the thrust coefficient
C_{IP} = in-plane forces modulus coefficient, $C_{IP} = F_{IP}/\rho_\infty n^2 D^4$
D = front propeller diameter (m)
dt = timestep (deg/iteration)
$\mathbf{e_x}, \mathbf{e_r}, \mathbf{e_\theta}$ = basis vectors of the rotating frame
F_{IP} = in-plane forces modulus, $F_{IP} = \sqrt{F_Y^2 + F_Z^2}$ (N)
$F_{Y,Z}$ = lateral, normal force component (N)
J = advance ratio
K_p = nondimensional pressure coefficient
M_∞ = freestream Mach number
n = frequency of propeller rotation (1/s)
p_∞ = freestream pressure (Pa)
r = radius (m)
R = radius of the front blade (m)
s = rotor-rotor axial spacing (m)
T = thrust (N)
u_x = axial induced velocity (m/s)
u_θ = orthoradial induced velocity (m/s)
V_∞ = freestream velocity (m/s)
$V_{x\infty}$ = X-component of the freestream velocity (m/s)
W_∞ = freestream velocity projected in the front rotor rotating frame (m/s)
y^+ = nondimensional size of the first cell from the wall

Greek Symbols

α = angle of attack between the propellers axis and free stream velocity (deg)
α_{loc} = local incidence for a given propeller blade at a given radius r (deg)
β_r = pitch angle of blade at r/R (deg)
$\theta_{F,R}$ = azimuthal position of a given blade for front/rear rotor (deg)
ξ = relative radius, $\xi = r/R$
ρ_∞ = freestream density (kg/m^3)
ψ_{IP} = angle of in-plane forces with (Oz) axis (deg)
Φ_R = relative flow angle at r/R (deg)
Ω = propeller rotation speed (rad/s)

Acronyms

CFD = computational fluid dynamics
CROR = contra-rotating open rotor
DTS = dual time stepping
LUSSOR = lower upper symmetric successive over relation
SA = Spalart–Allmaras
URANS = unsteady Reynolds-averaged Navier–Stokes
WTT = wind tunnel testing

References

[1] Hager, R. D., and Vrabel, D., 1988, "Advanced Turboprop Project," NASA SP Technical Report No. 495.
[2] Lanchester, F. W., 1916, *The Flying-Machine From an Engineering Standpoint*, Constable and Co., London.
[3] Harris, R. G., 1918, "Forces on Propeller Due to Sideslip," British Aeronautical Research Council, Technical Report No. 427.
[4] Glauert, H., 1919, "The Stability Derivatives of an Airscrew," British Aeronautical Research Council, Technical Report No. 642.
[5] Glauert, H., 1935, *Aeroplane Propellers, Miscellaneous Airscrew Problems*, (Aerodynamics Theory, Vol. IV), Springer, New York.
[6] Goett, H. J., and Pass, H. R., 1941, "Effect of Propeller Operation on the Pitching Moments of Single-Propellers Monoplanes," NACA Technical Report No. L-761.
[7] Ribner, H. S., 1945, "Propellers in Yaw," NACA Technical Report No. 820.
[8] Bober, L. J., Chaussee, D. S., and Kutler, P., 1983, "Prediction of High Speed Propeller Flows Fields Using a Three-Dimensional Euler Analysis," NASA TM Technical Report No. 83065.
[9] Wong, P., Maina, M., Forsey, C. R., and Bocci, A. J., 1988. "Single and Contra-Rotating High-Speed Propellers: Flow Calculation and Performances Prediction," ICAS No. 2.4.2.
[10] Nicoud, D., Brochet, J., and Goutines, M., 1989, "A Methodology Proposal to Design and Analyse Counter-Rotating High Speed Propellers," ASME Paper No. 89-GT-38.
[11] Denton, J., and Singh, U. K., 1979, "Time Marching Methods for Turbomachinery Flow Calculation," *Application of Numerical Methods to Flow Calculations in Turbomachines* (VKI Lecture Series), E. Schmidt, ed., von Karman Institute for Fluid Dynamics, Rhode-St-Genese, Belgium.
[12] Nallasamy, M., 1994, "Unsteady Blade Pressures on a Propfan: Predicted and Measured Compressibility Effects," J. Aircr., **31**, pp. 730–736.
[13] Bousquet, J.-M., and Gardarein, P., 2002, "Improvements on Computations of High Speed Propeller Unsteady Aerodynamics," Aerosp. Sci. Technol., **7**(6), pp. 465–472.
[14] Stuermer, A., 2008, "Unsteady CFD Simulations of Contra-Rotating Propeller Propulsion Systems," 44th AIAA/ASME/SAE/ASEE Joint Propulsion Conference and Exhibit, Hartford, CT, July 21-23, AIAA Paper No. 2008-5218.
[15] Zachariadis, A., and Hall, C. A., 2011, "Application of a Navier–Stokes Solver to the Study of Open Rotor Aerodynamics," ASME J. Turbomach., **133**(3), p. 031025.
[16] Peters, A., and Spakovszky, Z. S., 2012, "Rotor Interaction Noise in Counter-Rotating Propfan Propulsion Systems," ASME J. Turbomach., **134**(1), p. 011002.
[17] Schnell, R., Yin, J., Voss, C., and Nicke, E., 2012, "Assessment and Optimization of the Aerodynamic and Acoustic Characteristics of a Counter Rotating Open Rotor," ASME J. Turbomach., **134**(6), p. 061016.
[18] Stuermer, A., and Yin, J., 2011, "Installation Impact on Pusher-CROR Engine Low Speed Performance and Noise Emission Characteristics," 46th Applied Aerodynamics Symposium of Rotating Bodies, Orleans, France, March 28-30.
[19] Laban, M., Kok, J. C., and Prananta, B. B., 2010, "Numerical Tools for Contra-Rotating Open-Rotor Performance, Noise and Vibration Assessment," 27th International Congress of the Aeronautical Sciences (ICAS 2010), Nice, France, September 19-24.
[20] Brandvik, T., Hall, C., and Parry, A. B., 2012, "Angle-Of-Attack Effects on Counter-Rotating Propellers at Take-Off," ASME Paper No. GT2012-69901.
[21] Ortun, B., Boisard, R., and Gonzalez-Martino, I., 2012, "Assessment of Propeller 1P-Loads Predictions," Int. J. Eng. Syst. Model. Simul., **4**, pp. 36–46.
[22] Dequin, B., Kampa, A. M., Grunhagen, K., Basset, P. M., and Gimonet, B., 2000, "HOST: A General Helicopter Tool for Germany and France," 56th Annual Forum of the American Helicopter Society, Virginia Beach, VA, May 2-4.
[23] Cambier, L., Heib, S., and Plot, S., 2013, "The Onera *elsA* CFD Software: Input From Research and Feedback From Industry," Mech. Ind., **14**(03), pp. 159–174.
[24] Kok, J. C., 2000, "Resolving the Dependence on Freestream Values for the k–ω Turbulence Model," AIAA J., **38**, pp. 1292–1294.
[25] Kok, J. C., 2009, "A Higher-Order Low-Dispersion Symmetry-Preserving Finite-Volume Method for Compressible Flow on Curvilinear Grids," J. Comput. Phys., **228**, pp. 6811–6832.
[26] Jameson, A., Schmidt, R. F., and Turkel, E., 1981, "Numerical Solutions of the Euler Equations by Finite Volume Methods Using Runge-Kutta Time Stepping," AIAA Paper No. 1981-1259.

[27] Jameson, A., 1991, "Time Dependent Calculations Using Multigrid, With Applications to Unsteady Flows Past Airfoils and Wings," AIAA Paper No. 91-1596.
[28] Spalart, P. R., and Allmaras, S. R., 1992, "A One-Equation Turbulence Transport Model for Aerodynamic Flows," 30th AIAA Aerospace Sciences Meeting and Exhibit, Reno, NV, January 6-9, AIAA Paper No. 92-0439.
[29] Yoon, S., and Jameson, A., 1987, "An LUSSOR Scheme for the Euler and Navier–Stokes Equations," AIAA J., **4**, pp. 36–46.
[30] Jameson, A., and Yoon, S., 1986, "Multigrid Solution of the Euler Equations Using Implicit Schemes," AIAA J., **24**(11), pp. 1737–1743.
[31] Couaillier, V., 2005, "Effective Multidimensional Non-Reflective Boundary Condition for CFD Calculations Applied to Turboengine Aeroacoustics Prediction," ISABE 17th Symposium on Air Breathing Engines (ISABE 2005), Munich, Germany, September 4-9.
[32] Boisard, R., Delattre, G., and Falissard, F., 2011, "Assessment of Aerodynamics and Aero-Acoustics Tools for Open Rotors," 9th European Turbomachinery Conference, Istanbul, Turkey, March 21-25, pp. 21–25.
[33] Negulescu, C. A., 2013, "Airbus AI-PX7 CROR Design Features and Aerodynamics," SAE 2013 AeroTech Congress & Exhibition, Montreal, Canada, September 24-26, SAE Paper No. 2013-01-2245.
[34] Rai, M., 1986, "A Conservative Treatment of Zonal Boundaries for Euler Equation Calculations," J. Comput. Phys., **62**, pp. 472–503.
[35] Fillola, G., Le Pape, M.-C., and Montagnac, M., 2004, "Numerical Simulations Around Wing Control Surfaces," 24th International Congress of the Aeronautical Sciences (ICAS 2004), Yokohama, Japan, August 29-September 3.
[36] Gourdain, N., Montagnac, M., Wlassow, F., and Gazaix, M., 2010, "High-Performance Computing to Simulate Large-Scale Industrial Flows in Multistage Compressors," Int. J. High Perform. Comput. Appl., **24**(1), pp. 429–443.
[37] Tyler, J. M., and Sofrin, T. G., 1962, "Axial Flow Compressor Noise Studies," SAE Trans., **70**, pp. 309–332.
[38] Purwanto, A., Deconinck, T., Vilmin, S., Lorrain, E., and Hirsch, C., 2011, "Efficient Prediction of Nacelle Installation Effects at Take-Off Conditions," 9th European Turbomachinery Conference, Istanbul, Turkey, March 21-25.